Published in final edited form as:
*Nucl Med Biol*. 2013 April ; 40(3): 351–360. doi:10.1016/j.nucmedbio.2013.01.001.

# Heptamethine Cyanine Based $^{64}$Cu - PET Probe PC-1001 for Cancer Imaging: Synthesis and In Vivo Evaluation

**Li Xiao**[1,2,§], **Yi Zhang**[1,§], **Wei Yue**[3], **Xiuzhen Xie**[1], **Ji-ping Wang**[3], **Mahendra D. Chordia**[2], **Leland W.K. Chung**[4,*], and **Dongfeng Pan**[1,*]

[1]Department of Radiology, University of Virginia, Charlottesville, VA 22908, USA

[2]Department of Chemistry, University of Virginia, Charlottesville, VA 22908, USA

[3]Department of Endocrinology and Metabolism, University of Virginia, Charlottesville, VA 22908, USA

[4]Uro-Oncology Research, Samuel Oschin Comprehensive Cancer Institute, Cedars-Sinai Medical Center, Los Angeles, California 90048, USA

## Abstract

**Purpose—**Development of a heptamethine cyanine based tumor-targeting PET imaging probe for noninvasive detection and diagnosis of breast cancer.

**Methods—**Tumor-specific heptamethine-cyanine DOTA conjugate complexed with Cu-64 (PC-1001) was synthesized for breast cancer imaging. *In vitro* cellular uptake studies were performed in the breast cancer MCF-7 and noncancerous breast epithelial MCF-10A cell lines to establish tumor specificity. *In vivo* time-dependent fluorescence and PET imaging of breast tumor xenografts in mice were performed. Blood clearance, biodistribution, and tumor-specific uptake and plasma binding of PC-1001 were quantified. Tumor histology (H&E staining) and fluorescence imaging were examined.

**Results—**PC-1001 displayed similar fluorescence properties ($\varepsilon$=82,880 $cm^{-1}M^{-1}$, $E_x$/$E_m$=750/820 nm) to the parental dye. Time-dependent cellular accumulation indicated significantly higher probe uptake (>2-fold, 30 min) in MCF-7 than MCF-10A cells and the uptake was observed to be mediated by organic anion transport peptides (OATPs) system. *In vivo* studies revealed that PC-1001 has desirable accumulation profile in tumor tissues, with tumor versus muscle uptake of about 4.3 fold at 24 h and 5.8 fold at 48 h post probe injections. Blood half-life of PC-1001 was observed to be 4.3±0.2 h. Microscopic fluorescence imaging of harvested tumor indicated that the uptake of PC-1001 was restricted to viable rather than necrotic tumor cells.

**Conclusions—**A highly efficient tumor-targeting PET/fluorescence imaging probe PC-1001 is synthesized and validated in vitro in MCF-7 breast cancer cells and in vivo in mice breast cancer xenograft model.



*Corresponding authors: Dongfeng Pan, PhD Department of Radiology, University of Virginia Rm 263, 480 Ray C. Hunt Dr, Snyder Bldg, Charlottesville, VA, 22908 Phone: (434) 243-2893; Fax: (434) 924-9435; dp3r@virginia.edu Leland W.K. Chung, PhD Uro-Oncology Research, Samuel Oschin Comprehensive Cancer Institute, Cedars-Sinai Medical Center, Los Angeles, CA 90048 Phone: (310) 423-8431; Fax (310) 423-8300; Leland.Chung@cshs.org.
§These authors are equally contributed to this work.

**Keywords**

Breast cancer; Cu-64; PET imaging probe; tumor-targeting; xenograft

## INTRODUCTION

Cancer diagnosis and treatment are the most demanding challenges facing clinicians and scientists because of the lack of appropriate agents that can be used for early cancer detection and followup of progression of disease, and respond to treatment for therapeutic intervention. Molecular imaging approaches could offer effective tools for cancer detection and prognosis allowing visualization of tumors in real time and space [1]. Because of the lack of universal cancer specific targets, new highly sensitive molecular probes are needed for precise detection of various cancer types [2, 3].

The importance of early cancer detection is evident. In a study of 5-year survival results, over 90% of patients survived when the disease was detected in the beginning at the onset of tumor [4]. A variety of diagnostic imaging techniques, such as magnetic resonance imaging (MRI), nuclear imaging [positron emission tomography (PET), single photon emission computed tomography (SPECT)], ultrasound (US) and optical imaging are being developed and utilized for tumor detection and visualization [2, 5, 6], however, there is still unmet need for highly tumor specific probes with optimal pharmacological properties. For example, PET is a very sensitive, non-invasive, biological function dependent technology widely utilized in pre-clinical and clinical imaging of cancer [7, 8], but direct development of PET imaging probe is impeded by poor resolution at cellular level and exposure to the hazardous radioactivity at every step. Intrinsic near infrared fluorescence (NIRF) properties offered by a dye along with PET probe would overcome these difficulties. In addition NIRF optical imaging has the capability to provide detailed information at the molecular and cellular level over a long period. NIRF, however, has limited ability to present quantitative 3D images due to poor light penetration through deep tissues [9-11]. Thus combination of both nuclear and optical techniques will facilitate the development of efficient probes for cancer imaging. The probe would also overcome the limitations of complementary singular techniques. Currently, multi-modality imaging techniques are garnering significant interest, thus variety of probes are being developed for various targets to monitor tumor and other diseases [12-15]. The present investigation focuses on the development of a PET/fluorescence imaging probe for the visualization of human breast cancers from deep tissues that has potential to be applicable to numerous cancers. Previous studies report discovery of a class of carbocyanine dye, heptamethine cyanine, which allowed detection of human and mouse tumors with high degree of sensitivity and specificity [3, 5, 16].

Recently Yang *et al* [17] and others [11] reported a class of heptamethine cyanine dyes that yields tumor-specific NIRF signals for the detection of a broad-spectrum of human and mouse tumor cell lines, tumor xenografts and mouse tumors from transgenic animals. To further improve the sensitivity and clinical utility of this class of cyanine dye for deep-tissue detection of tumors, we modified the dye by conjugating with a positron emitting radionuclide and tested its feasibility in cultured human breast cancer cells and breast tumor xenografts in mice. The dye MHI-148 was chosen because of its high tumor-specificity. This feature of MHI-148 allowed us to monitor tumor progression, including metastases to bone and visceral organs in host mice [17]. In this study we synthesized PET/NIRF probe PC-1001 (**4b**), by conjugating MHI-148 with a DOTA chelator and subsequent chelating with Cu-64 for independent PET and fluorescence imaging. This two-component probe is the first example of novel tumor specific fluorescent dye with both targeting and detection properties in one component, and the second component DOTA-Cu-64 with capability to

perform nuclear imaging. In contrast all other multimodal probes reported to date, the tumor targeting component is separate than that of the detection part and thus need minimum of three components. The NIRF property of the probe can be used in early stages of the development of the probe for in vitro / in vivo optimization of parameters and its validity prior to final live animal PET imaging. The positron emitting property of the probe can then provide high sensitivity and deep tissue spatial resolution for initial detection of primary tumors and their metastatic lesions. Tumor size can then be monitored overtime with NIRF imaging. Here in we describe the detailed method and development of such probe PC-1001 for cancer imaging in the breast tumor xenograft model.

## MATERIALS AND METHODS

All chemicals purchased commercially were of analytical grade and were used without further purification. 1,4,7,10-Tetraazacyclododecane-1,4,7,10-tetraacetic acid (DOTA) was obtained from Macrocyclics, Inc (Dallas, TX, USA). 3-(4,5-Dimethylthiazol-2-yl)-2,5-diphenyltetrazolium bromide (MTT) was purchased from Invitrogen (Grand Island, NY, USA). All other chemicals were purchased from Sigma-Aldrich Chemical Co (St. Louis, MO, USA). C-18 Sep-Pak cartridge (product #: WAT023501) for tracer purification was obtained from Waters Corporation (Milford, MA). $^{64}Cu$-$CuCl_2$ (half-life, 12.7 h; $\beta^+$, 17.8%, $E_{\beta+max}$, 656 keV; $\beta^-$,38.4%, $E_{\beta-max}$, 573 keV) was purchased from Washington University (St. Louis, MO, USA). Ultrapure water (resistivity, 18.2 MΩ cm) used for making solutions was obtained from Milli-Q Direct Ultrapure Water System from Millipore (Billerica, MA, USA). High-performance liquid chromatography (HPLC) grade solvents were purchased from Fisher Scientific (Pittsburgh, PA, USA). Chemistry and radiochemistry products were analyzed and purified by preparative and semi-preparative reversed-phase HPLC. HPLC was performed on a Varian ProStar system (models: pumps, 210; column valve module, 500; fraction collector, 701) (Varian Instruments) equipped with either a DENALI™ 238 DE C18 SPRING preparative column (120 Å, 250×25 mm) and an Alltech Apollo C18 semi-preparative column (5 μm, 250×10 mm) (Grace Davison Discovery Sciences) and ABI Spetroflow 783 UV detector as well as a NaI solid scintillation Flow Count Radio-HPLC detector (Bioscan). Two mobile phases were used for HPLC: Solvent A (0.1% TFA in water) and Solvent B (0.1% TFA in 80% aqueous acetonitrile). The mobile phase gradient varied according to characteristics of compounds for 30 min at a flow rate 12 mL/min for the preparative column and 3 mL/min for the semi-preparative column monitored at 254 nm. Matrix-assisted laser desorption/ionization time-of-flight mass spectroscopy (MALDI-TOF-MS) analysis was performed on compounds at the W.M. Keck Biomedical Mass Spectrometry Laboratory using a Bruker Daltonics system at the University of Virginia. $^1H$ and $^{13}C$ nuclear magnetic resonance (NMR) spectra were recorded on Varian Innova spectrometer (300 MHz).

MCF-7 cells (originally provided by Dr. R. Bruggemeier, Ohio State University) were grown in IMEM containing 5% fetal bovine serum (FBS) (Invitrogen) and 1% penicillin/streptomycin (GIBCO) [18]. MCF-10A cells are an immortalized, non-transformed epithelial cell line derived from human fibrocystic mammary tissue and was purchased from American Type Culture Collection (ATCC). MCF-10A cells were cultured in DMEM/F12 medium supplemented with epidermal growth factor 40 ng/ml (BioVision), insulin 10 μg/ml (Sigma), hydrocortisone 500 ng/ml (Sigma), cholera toxin 100 ng/ml (Calbiochem), 5% horse serum (Invitrogen), 1% penicillin and streptomycin. Unless otherwise mentioned, all cell lines were cultured in the incubator at 37°C in a 5% $CO_2$ humidified atmosphere ($CO_2$ water Jacketed incubator, series II, Forma Scientific). Phosphate buffered saline (PBS) (0.1 M, pH 7.45) was purchased from Invitrogen. Human serum albumin (HSA) was obtained from Sigma-Aldrich. Krebs-Henseleit (KH) buffer (118 mM NaCl, 23.8 mM $NaHCO_3$, 4.83

mM KCl, 0.96 mM $KH_2PO_4$, 1.20 mM $MgSO_4$, 12.5 mM HEPES, 5.0 mM glucose, and 1.53 mM $CaCl_2$, pH adjusted to 7.4) was prepared as reported [19, 20].

A breast tumor xenograft model was used for in vivo studies. Female athymic mice (3-4 weeks old) were obtained from Charles River Laboratory. The mice were handled and processed according to protocol approved by the University of Virginia Animal Care and Use Committee in accordance with current guidelines of National Institutes of Health Model Procedure of Animal Care and Use. MCF-7 breast tumor cells (ten million cells in 0.1 ml) suspended in Matrigel (BD Biosciences) were inoculated into the mammary gland fat pad of ovariectomized athymic mice (four inoculants per mouse; $n_t$=4). Tumor growth was supported by a subcutaneous Silastic capsule implant containing a mixture of 17-β-estradiol and cholesterol at a ratio of 1:3, which provided ~80 pg/ml of plasma 17-β-estradiol [18]. Tumor sizes were monitored by measuring tumor diameters with calipers (both length and width) once a week and tumor volumes were calculated using the formula $3/4\pi r_1{}^2 r_2$ where $r_1<r_2$[21]. Tumors were allowed to grow for 6-8 weeks before initiation of the studies. Mice with tumors of 150 $mm^3$ or above were used for *in vivo* experiments.

The probe solutions for injection were prepared in sterile PBS buffer (0.1 M, pH 7.45). Mice were administered with imaging probes (PBS volume 100-150 μL) by two different methods for blood collection, probe biodistribution, and fluorescence and PET imaging: 1) intravenous (iv) injection via mouse tail vein using a syringe (1/2 cc U-100 Insulin Syringe, 28G1/2, Fisher Scientific) under anesthesia (2% isoflurane in oxygen); 2) intraperitoneal (ip) injection via mouse lower abdominal area using the same syringe as described. Radioactive doses of probe PC-1001 (**4b**) for animal injection were prepared and measured with a well counter (CAPINTEC Radioisotope Calibrator CRC-7, code 115). Radioactive samples for partition coefficient analysis, *in vitro* cell studies, blood clearance and organ distribution were measured for radiation using an automatic gamma counter (2480 Wizard, PerkinElmer). Whole animal fluorescence imaging was performed by IVIS Spectrum (Caliper Life Science) and the PET scans were acquired using a microPET Focus 120 (Siemens Medical Solutions).

## Synthesis and radiolabeling of 4b

As described in Figure 1, the heptamethine cyanine dye MHI-148 (2-[2-[2-chloro-3-[2-[1,3-dihydro-3,3-dimethyl-1-(5-carboxypentyl)-2H-indol-2-ylidene]-ethylidene]-1-cyclohexen-1-yl]-ethenyl]-3,3-dimethyl-1-(5-carboxypentyl)- 3H-indolium bromide) (compound **1**, see Supplemental Figure 1 for detailed synthesis) and DOTA-SulfoNHS were synthesized according to a process described previously [17, 22, 23]. One of the carboxylic group of MHI-148 was conjugated with N-α-Boc-Lys-OH (50 mg, 0.2 mmol) through NHS-activation followed by deprotection of Boc using TFA to afford compound **2** that was purified by HPLC (70-100% Solvent B in 30 min) with a retention time of 12.3 min. The amine group of compound **2** (84.8 mg, 0.1 mmol) was conjugated with DOTA-SulfoNHS (116.3 mg, 0.2 mmol) to yield compound **3** (55.2 mg, yield 44.7%) which was purified by semi-preparative HPLC (60-100% Solvent B in 30 min) with a retention time of 12.3 min (Supplemental Figure 2a). Metal chelation of DOTA-complex **3** (100 μg) either by $CuCl_2$ for cold complex **4a** or by copper-64($CuCl_2$) (0.035 μg = 0.5 nmol, total activity 2 mCi, 74 MBq; 57 mCi/μg specific activity) yielded the final imaging probe PC1001 (**4b**) after purification by HPLC (60-100% Solvent B in 30 min) with a retention time of 14.3 min. using NaI solid scintillation Flow Count Radio-HPLC radiodetector (Bioscan). The single fraction from HPLC was concentrated by gently blowing positive flow of nitrogen (~2h). The residue left in test tube upon concentration was reconstituted in PBS buffer (1.0 mL) and radioactivity was measured (**4b,** total activity 1.8 mCi, 66.6 MBq, 0.45 nmol, ~90 % radiochemical yield) (Figure 1). The final concentration of apporx. 10 MBq /150 μL was

adjusted for mouse dosing. The chemical purity of probe **4b** cannot be ascertained by the analytical HPLC since no UV/visible peak was detectable, but the radio-HPLC data indicated a single peak (> 95%) and the data is provided in supplemental material (Supplemental Figure 2b). In similar way cold probe **4a** is synthesized with chemical yield and purity of > 95% after purification by HPLC. All intermediates and final products were purified by RP-HPLC to homogeneity, Structural characterization of compound **2** and **3** was performed by $^{1}H$ and $^{13}C$ NMR and compound **3** and **4a** were analyzed by MALDI-TOF-MS.

## Partition Coefficient (log *P*)

Freshly purified probe PC-1001 (**4b**, 185 kBq) by HPLC was dried over by blowing $N_2$ flow to remove TFA and acetonitrile, solubilized in 500 μL DI water and mixed with 500 μL of octanol in an Eppendorf tube (1.5 mL). The tube was sonicated for 10 min and centrifuged at 4000 rpm for 5 min (Marathon Micro-A, Fisher Scientific). Aliquots (100 μL) from the octanol and water layers were carefully removed. Radioactivities from both layers were measured with a gamma counter. Partition Coefficient (log *P*) was calculated by the following equation: $\log P = \log_{10}$ [(radioactivity in octanol)/(radioactivity in water)]. The measurement was recorded in triplicate and presented as an average.

## *In vitro* cellular studies

**Time-dependent cellular uptake of radioactive probe 4b—**MCF-7 and MCF-10A cells were pre-seeded in 48-well microplates with a density of ~$2 \times 10^5$ cells/mL (500 μL/well). After incubation at 37°C for 24 h, probe **4b** (74-111 kBq, 20 μL per well) was added into each well. Medium from selected wells was removed at various time points after probe addition (3, 5, 15, 20, 30 and up to 60 min), and those wells were then washed successively with KH buffer [19, 20] for three times. At the end of 60 min time point, lysis buffer (20 mM Tris and 0.4% Triton X-100, pH adjusted to 9.0) (500 μL) was added to all wells. The plate was gently shaken for 10 min (400 rpm, Labnet Shaker, National Labnet Laboratory). The lysate from each well was transferred to separate tubes and each well was washed with PBS buffer (500 μL) for two times, collected and combined with the lysate from the same well. Radioactivity of each tube was measured by gamma counter, with decay corrected to the time point of probe addition, normalized by protein content, and plotted against incubation time using Prism 5.0 (GraphPad). The protein amounts (mg) of cell lysates were determined using a standard BCA (bicinchoninic acid) Protein Assay Kit (Pierce, Thermal Fisher Scientific Inc., Rockford, IL) following the product manual. A 96-well microplate reader (SPECTRAmax 190; Molecular Devices) was used to measure the absorbance of assay solution at 562 nm. All measurements were conducted in triplicate and reported as an average ± SD.

**Mechanism-based cellular uptake of radioactive probe 4b—**MCF-7 and MCF-10A cells were pre-seeded on 48-well microplates with a density of ~$2 \times 10^5$ cells/mL (500 μL/well) and incubated for 24 hours. Both cell types were divided into three groups as 1) control, 2) inhibitor addition and 3) for determination of the effects of temperature in separate well plates. Each group was first processed as follows: Group 1) addition of blank PBS buffer; Group 2) addition of a uptake inhibitor, bromosulfophthalein (BSP) (250 μM as final concentration), which is known to block organic anion transport polypeptides (OATPs) [24-26]; Group 3) addition of blank buffer and incubation at lower temperature (0°C) with probe **4b** (74-111 kBq/well) for 30 min, respectively. At the end of incubation, supernatants were removed and each well was washed with KH buffer for three times. The cells were lysed and processed as described in the previous experiment. Radioactivity of each tube was measured by gamma counter, decay corrected to the time point of probe addition, normalized to per mg of protein. The measurement was performed in triplicate and reported

as an average ± SD. The control MCF-7 cell uptake was assigned as 100% and was used as standard.

### Blood Clearance

PC-1001 (0.74-1.11 MBq/~20 g mouse) was injected into tail vein of tumor-bearing mice ($n$=4). Approximately 30-50 μL of blood from the contralateral tail vein was collected in capillary tubes at 5, 15, 30, 60, 180, 360 and 1280 min post probe injection. The capillaries were placed in pre-weighed tubes to measure the weight and radioactivity of the blood withdrawn. Radioactivity from each sample was measured by a gamma counter with radioactivity decay corrected to the time of probe injection, normalized for injected dose and blood weight, and expressed as percentage injected dose per gram blood (%ID/g). The data obtained was processed with OriginPro 7.5 (OriginLab Corp.).

### Biodistribution

Tumor and organ distribution of probe **4b** was determined in five groups of tumor-bearing mice (number of mice; $n$=4, number of tumors; $n_t$=16, each mouse was bearing 4 tumors). Mice were given intravenous (3 groups) or intraperitoneal (2 groups) injection with probe **4b** (1.11-1.85 MBq) and results were categorized based on post probe injection time (6, 24, and 48 h pi) and route of probe administration (iv or ip). At various time points post injection, a single blood sample was taken from the tail vein and mice were euthanized by deep halothane anesthesia immediately. Organs and tissues (tumors, heart, lungs, muscle, bone, liver, kidney, spleen, small intestine, and stomach) were harvested, rinsed with PBS buffer, wiped with filter paper and weighed in a pre-weighed tube for the gamma counter measurements. The radioactivity of each sample was measured, decay corrected to the injection time, normalized for injected dose and organ/tissue weight, and expressed as percentage injected dose per gram tissue (%ID/g). The results were categorized based on post probe injection time (6, 24, and 48 h pi) and route of probe administration (iv or ip).

### *In vivo* imaging protocol

**Fluorescence imaging—**A group of tumor-bearing mice ($n$=4, $n_t$=16, each mouse bearing four tumors) were iv injected with 10 nmol of probe **4a** (in 100 μL PBS) and *in vivo* NIRF imaging of mice was performed at various time points (1, 3, 6, 24, 48, 72 and 168 h pi) with a filter pair of $E_x/E_m$=745/820 nm. Identical illumination settings (auto exposure, medium binning, F/Stop=2) were used for acquiring all images. The fluorescence emission was normalized to photons per second per centimeter squared per steradian (p/s/cm$^2$/sr). Images were acquired and analyzed by Live Image 4.0 (Caliper Life Science), and displayed in the same scale of fluorescence intensity. The fluorescence emission was measured from the region of interest (ROI) of all four tumor inoculants as well as from the muscle of the hind legs as control. For all the time points, fluorescence intensity of tumor was presented as an average of all tumors ($n$=4, $n_t$=16) in each group. Fluorescence intensity of muscle was shown as an average of four mice. Both fluorescence intensities for tumor and muscle were plotted in a time-dependent manner using Prism 5.0 software package.

**PET imaging—**Tumor-bearing mice were administered with probe **4b** (8.88-9.62 MBq, 0.06-0.065 nmol, ~150 μL in PBS per ~20g mouse) via iv ($n$=2, $n_t$=8) and ip ($n$=2, $n_t$=8) injections. Small-animal PET scan was performed on each animal at various time points (3, 6, 24, and 48 h pi). For blocking experiment mixture of 500 μg of cold complex **4a** with PET probe **4b** (11.0 MBq) was used for mouse injection. Acquisition time for each scan was 10 min for 3h and 6h, 20 min for 24 h and 30 min for 48 h time points. PET data for were reconstructed with the OSEM3D/MAP algorithm (zoom factor, 2.164) using microPET Manager (version 2.4.1.1, Siemens). The reconstructed pixel size was 0.28 × 0.28 × 0.79

mm on a 128 × 128 × 95 image matrix. All PET images were corrected for decay but not for attenuation. Each image analysis was performed using ASIPRO software (Siemens). To characterize the accumulation of probes in tumors, region-of-interest (ROI) analysis was performed manually by visualizing the tumor sites as they appeared as bumps under the skin to identify the radioactivity originating in the tumor region. For both probes at all time points, 8-10 contiguous transaxial tumor ROIs were drawn to cover the entire tumor region, and standardized uptake values (SUVs) were computed using the following formula: SUV=([nCi/cc] × [animal weight (g)] / injected dose (nCi) [27].

### Distribution of probe in blood

Probe **4b** was injected at a dose of 9.2 MBq per 20 g mice via tail vein. At 6 h pi, blood (~200 μL) was collected from each mouse ($n$=3) by cardiac puncture using syringes and Eppendorf tubes (1.5 mL) pre-rinsed with heparin (10 U/mL in PBS). Half of the blood (~100 μL per mouse) was transferred to gamma counter tubes to measure the radioactivity of whole blood and the other half (~100 μL per mouse) was centrifuged at 3000 rpm for 5 min (Eppendorf Centrifuge 5810R, Brinkmann Instruments, Inc). From the centrifuged sample, supernatant (majority of serum, >90 μL) was collected from the settled red blood cells (RBC) and transferred to separate tubes. Both the supernatant and RBC were measured for radioactivity. Radioactivity of all samples for each mouse were normalized by the value of whole blood (100%) and binding data of each blood component was averaged for three mice (%).

### Histological analysis

The mice treated with probe **4a** (10 nmol per ~20g mice) were euthanized to harvest the tumors. The harvested tumors were cut into two sections and fluorescence imaging by IVIS Spectrum was performed as described above. The fluorescence imaged tumors were further used for histological analysis. Tumors were fixed by immersing into 10% neutral buffered formalin solution for 48 h before transferring to 70% ethanol. The fixed tissues were dissected to adjacent histological sections (5 μm thick) that were stained with hemotoxylin and eosin (H&E staining) while keeping two consecutive slice blank (no staining) for direct microscopic visualization of fluorescence signal. H/E stained slices were observed under a light microscope (Zeiss PrimoStar) with a camera (Zeiss AxioCam Cc1) and pictures on ROI were recorded by AxioVision 4.8 (Zeiss). Meanwhile blank slices consecutive to the H&E stained ones were examined on a confocal microscope (Olympus IX81 microscope) equipped with a Hamamatsu digital camera ORCA-ER, with a laser excitation filter of 633 nm and long pass emission filter of 650 nm. The probe distribution and accumulation in tumor was acquired at a microscopic level.

### Statistics

Quantitative data are expressed as means ± standard deviation (SD). For statistical classification, a Student t test (2-tailed, unpaired) was performed using Prism 5.0 software (GraphPad). Any P value less than 0.05 was considered statistically significant.

## RESULTS

### Synthesis and Characterization of probe 4b

As shown in Fig. 1, the dual-modality imaging probe consisted of three modules: tumor-targeting carrier (NIRF dye), linker and a radio-metal chelating moiety. PC-1001 was synthesized in three straightforward chemical steps. At each step, the intermediates were purified by HPLC and the compounds were characterized by NMR and MALDI-TOF mass analysis. $^{1}$H and $^{13}$C NMR of compounds **2** and **3** are presented in Supplemental Figures 3,

4 and 5. MALDI-TOF analysis of compound **3** and **4a** exhibited similar mass spectra with a [$M^+$] peak of 1197.648 (Supplemental Figure 6). The final radiolabeled probe **4b** exhibited a single peak by HPLC with a radio-purity more than 95%, and was compared with its non-radioactive counterpart **4a** by co-elution experiment for confirmation of the structure (Supplemental Figure 2c).

The log *P* value of **4b** was calculated to be 1.25±0.20.

## Spectrum properties

The molar extinction coefficient (ε) of **4a** was measured to be 82,880 $cm^{-1}M^{-1}$ at the wavelength of 750 nm (MHI-148 **1**, ε=55,320 $cm^{-1}M^{-1}$). As shown in Supplemental Figure 7A, the optimal excitation wavelength of probe **4a** was 750 nm, which was used for all subsequent studies. Fluorescence spectra of **4a** demonstrated enhanced intensity after mixing with various concentrations of human serum albumin (HSA) and the fluorescence intensity ($E_m$=820 nm) reached peak value when the HSA concentration was 0.5% (~2 fold increase) compared to that of no HSA in the system (Supplemental Figure 7B). The fluorescence intensity of both probe **4a** and MHI-148 **1** (the carrier molecule) demonstrated a linear increasing correlation with the probe concentration within the range of 0-10 μM (Supplemental Figure 7C). However an inverted decreasing trend was exhibited when the probe concentration was beyond 10 μM (data not shown). This information provided a concentration range for probe dosing for *in vivo* fluorescence imaging. The fluorescence emission spectra of **4a** was also measured under a series of pH conditions (pH=4.0, 5.0, 5.8, 6.2, 6.6, 7.0 and 7.4) and observed to be independent of pH (Supplemental Figure 8).

## *In vitro* cellular uptake

The comparative cancer and noncancerous cellular uptake was measured and quantified by the radioactivity amount of the more sensitive PET probe **4b** in the cells. Fig. 2a depicts time-dependent uptake of probe **4b** in MCF-7 and MCF-10A cells. MCF-10A cells exhibited a slow but steady probe uptake over the entire incubation period (60 min). In contrast, probe uptake in MCF-7 cells showed rapid accumulation in the initial 30 min and then a steady increasing trend (> 2 fold higher compared to noncancerous MCF-10A cells) until 60 min post probe incubation. The preliminary mechanism-based cellular uptake study was performed (Fig. 2b). At 30 min post incubation, probe accumulation in control MCF-7 cells (100%) was 3 fold higher than that of MCF-10A (34±2%) ($P<0.0001$). Probe uptake in MCF-7 cells with an OATP inhibitor, BSP, was decreased to 55±6% ($P<0.0001$). In contrast, treatment with BSP did not affect probe uptake in MCF-10A cells ($P>0.05$), suggesting the probe uptake by noncancerous breast epithelial cells is OATP-independent. In addition, the effect of temperature on cellular uptake of **4b** was studied, and showed that in both cell lines the cellular uptake decreased with lowering temperatures (MCF-7 at 0°C, 64±13%, $P<0.0001$ when compared to control MCF-7, 100% at RT ; MCF-10A at 0 °C, 9±1%, $P<0.001$ when compared to control MCF-10A, 34±2% at RT).

## *In vivo* NIRF imaging

*In vivo* uptake of probe **4a** in tumor-bearing mice was monitored by NIRF imaging as described in Materials and Methods. The corresponding analysis provided a preview of the pharmacokinetic profile of probe prior to evaluation of radioactive probe **4b** for PET imaging. As noted in Fig. 3a and Fig. 3b, the contrast for tumors started to be visibly distinct by fluorescence imaging as soon as 1 h pi. Tumor fluorescent intensity increased rapidly and peaked at 48 h subsequently remained at high levels for the period of 168 h (7 days). In contrast, the fluorescence intensity of muscle indicated a slower uptake rate during the first 24 h pi and over rest of the time. The muscle uptake of probe **4a** reached a plateau at 48 h

with fluorescence intensity ~4 fold less than that in the tumor and then decreased steadily thereafter.

## PET imaging and analysis

Based on the data obtained from fluorescence imaging of tumor for probe **4a**, a window of opportunity for nuclear imaging was determined. PET was then performed in that time frame using probe **4b** to achieve an optimum contrast. As described in the experimental section, *in vivo* PET imaging data was collected at various time points (3, 6, 24 and 48 h pi) and SUV were computed. Representative PET images at 24 and 48 h pi are shown in Fig. 3c. SUV data [tumor to muscle uptake ratios were 0.63:0.33, 0.64:0.36, 0.94:0.22, and 1.07:0.19 for time points of 3, 6, 24 and 48 h pi, respectively] are presented in Fig. 3d. Blocking experiment was performed using cold tracer (excess >100 fold) with the similar quantity of PET probe **4b** (~11 MBq) and 24 h pi images were acquired and compared with similar time point with PET probe imaging. The tumor to background SUV ratio was observed to be 3.02±0.327 by probe **4b** in PET imaging, while for blocking experiment the same SUV ratio was observed to be 1.400±0.103. The images of slices of blocking experiment and its comparison with PET imaging, followed by ROI analysis and SUV measurements as described in method section is presented in Supplemental Figure 9.

## Blood Clearance and Biodistribution

The radioactivity of blood withdrawn at various time points was measured and fitted into a mono-exponential equation, $y = y_0 + A_1 \times \exp[-(x-x_0)/t_1]$ with $R^2 = 0.9794$. The blood clearance data is presented as the inset of Fig. 4a. The elimination half-life for blood clearance ($T_{1/2}$) was calculated to be 4.3±0.2 h.

The tumor and organ uptake profile of probe **4b** at various post injection time points and via different injection routes is shown in Fig. 4a. The majority of probe radioactivity was retained in the blood at 6 h pi (0.73±0.04 %ID/g), which then dramatically decreased until 24 h pi (0.34±0.04 %ID/g for iv and 0.38±0.11%ID/g for ip injection, ~50% elimination). Later on the radioactivity appeared to remain constant in blood through 48-h pi, irrespective of injection route. The probe **4b** demonstrated a much higher rate of tumor-specific uptake and accumulation over time (0.14±0.02 %ID/g at 6 h for iv, 0.16±0.03 %ID/g at 24 h for iv, 0.25±0.05 %ID/g at 24 h for ip, 0.27±0.08 %ID/g at 48 h for iv, and 0.30±0.04 %ID/g at 48 h for ip). On the other hand, organs such as heart, liver, lungs and spleen exhibited much slower rates of uptake with time, and in kidney, muscle and bone, the amount of probe accumulation remained constant over time. The tumor to blood ratio of probe **4b** over a time period of 48 h pi increased more than 4 folds from ~0.2 to ~0.9. The data is presented in Supplemental Figure 10.

The radioactivity of both serum (~90%) and RBC (<10%) components of the blood was measured and normalized to whole blood (100%). The majority of radioactivity was observed to be associated with serum as exhibited in Fig. 4b.

## Correlation of probe accumulation with tumor size

The amount of radioactivity for various tumors in each individual mouse ($n$=20, $n_t$=80) was measured and decay corrected to the probe injection time point. Mice were randomly selected from various batches and separate time points, independent of route of probe administration. Analysis of all four sizes of tumors from each of these mice was performed and all mice showed a similar correlation between probe accumulation and tumor weight. Data for a representative mouse is shown in Fig. 4c, suggesting that probe accumulation (measured as whole tumor radioactivity, Bq) linearly correlated with individual tumor weights (g) ($R^2$=0.9837).

### Histological analysis

As depicted in Fig. 5a viable (V) and necrotic (N) tumor regions were distinguished visually and macroscopically. Viable tumor regions were pinkish in color whereas the necrotic areas were off-white or light pinkish. The fluorescence signals were mainly emitted from viable tumor regions while the necrotic parts showed little or no fluorescence signal (Fig. 5a and Fig. 5b). Microscopically, viable and necrotic tumor cells (darker nucleus) were identified by their characteristic morphology of H&E staining as shown in Fig. 5c (see more details in Supplemental Figure 11). The adjacent non-stained slices were observed under a fluorescence microscope to confirm the signal was mainly emitted from the viable tumor and not from the necrotic regions (Fig. 5c and Fig. 5d).

## DISCUSSION

Although in cancer research the molecular imaging is routinely used for detection and diagnosis of variety of tumors, its application in clinical practice, however, is still in infancy. There have been tremendous advances made recently towards obtaining more accurate, sensitive molecular imaging probes but these efforts are impeded by poor understanding of biology of disease and its variance in the initiation, progression and pathophysiology at individual level. In addition to the complex nature of disease, lack of specific target based molecules with well established mechanism of action limits the development of simple, highly sensitive tool for cancer in real time and space. Over the last few years due to advancement of computation and imaging in terms of power and resolution along with our understanding of biochemical pathways at molecular level aided in developing multiple probes and tools for cancer e.g. , MRI, CT, and gamma imaging. Each technique offers unique capability to detect and diagnose disease. Positron emission tomography (PET) is one of the highly sensitive, commonly used techniques for imaging variety of pathophysiological conditions. Many radiolabeled molecules were synthesized as molecular imaging probes and are currently in various phases of development, for example, RDG probes for angiogenesis [28], Cu-ATSM for hypoxia [29], ML-10 for apoptosis [30], FLT for cell proliferation [31]. Since each of these probes has its limitation for detection of cancer, there is unmet demand in discovering new universal probes with improved sensitivity, specificity for cancer. The development of PET probe, however, is highly complex, costly and tedious process. By having intrinsic fluorescent characteristics associated with PET probe one may able to expedite early phases of development of probe in research by implementing nonradioactive, low cost optical imaging mode of the probe. The dual-modality probe which once optimized can be radiolabeled at ease and used directly for imaging in live animal or fast forward to clinical studies.

Traditionally, NIRF compounds such as Cy 7 and IR dye 800 are used as optical imaging probes that are usually conjugated with other carrier systems for target site-specific delivery and detection of biological disturbances [9, 12, 13]. A variety of delivery systems have been developed in preclinical and clinical settings for monitoring pathophysiological changes using peptides, proteins/monoclonal antibodies (mABs), liposome and polymers [9, 32-35]. However, the application of these delivery systems to carry imaging probes has met with severe difficulties due to physiological barriers [36] such as spatial and temporal blood flow, vascular permeability and heterogeneous tissue distribution. Moreover, large molecule carrier systems have sample preparation, chemical/biological stability and storage issues associated with their clinical development. Small molecule tumor-specific delivery agents on the other hand can offer several advantages: i) ease of chemical modification to achieve optimal pharmacological properties, ii) ease of storage and handling due to their chemical stability, iii) high permeability across cell membranes, and iv) cost effectiveness.

The probe **4b** was synthesized with the goal of expediting development of molecular imaging of cancer in live animal with precision and high sensitivity. Realizing complementary properties of each NIRF and PET modality, and considering the intrinsic limitations of the NIRF agent the PET module is included in cyanine based dye MHI-148 which has shown excellent cancer cell uptake. The probe design consists of a novel two-component system, wherein the dye plays both tumor targeting and fluorescence detection roles, and the Cu-DOTA part permits nuclear imaging. Probe **4a** (non radioactive) as analyzed by UV/Vis spectroscopy showed an enhanced molar extinction coefficient compared with MHI-148, suggesting that conjugation with DOTA-Cu is not deleterious for probe design. Both the *in vitro* cellular uptake study and the *in vivo* imaging study suggested that modification of the dye structure with linker and Cu-DOTA moiety did not affect the tumor-targeting property of the dye carrier.

Probe **4a** exhibited a significant (> 2 fold) fluorescence enhancement after mixing with HSA as described in Supplemental Figure 6B. Meanwhile, the distribution profile of probe **4b** in blood (Fig. 4b) suggested that the majority of the probe was associated with serum and not with red blood cells. Concurrently, both results indicated the interaction between the probe and the protein (albumin) may be a factor contributing to longer half-life (4.3±0.2 h) (top inset of Fig. 4a) of **4b** in blood circulation and may be a reason for improving tumor-specific uptake over time [37]. *In vitro* cellular uptake studies indicated the selectivity for tumor cells (MCF-7) uptake of probe **4b** compared with noncancerous breast epithelial cells (MCF-10A) by radioactivity measurement as exhibited in Fig. 2a. Furthermore, the preliminary mechanistic studies (Fig. 2b) demonstrated that OATP may be an important transporter responsible for the active transport of the probe across cell membrane [17] (Fig. 2a and Fig. 2b).

The acquired fluorescence imaging data over a long period of time (up to 5 day pi) provided information of the pharmacokinetic profile for probe **4a**. Since PET imaging is mainly limited by the decay of the radioisotope, the long term evaluation of pharmacokinetic properties could not be performed by nuclear imaging. At 24 and 48 h pi, PET/NIRF imaging revealed a ~4.27 and 5.78 fold (for PET) and 2.71 and 3.54 fold (for NIRF) increase in intensity of signal in tumor compared with muscle tissue. Both fluorescence and nuclear imaging techniques indicated significant tumor uptake of probe **4a** and **4b** over time, indicating a similar selective accumulation trend in tumor (Fig. 3) validating promising potential of probe for cancer imaging. In addition from blocking experiment it has been established that the dual probe **4b** is exhibiting tumor specific uptake, when 100 fold more cold probe **4a** is mixed with PET probe **4b** and injected in mouse SUV ratio of tumor to background was 1.400± 0.103 (~0.4 more for tumor than background) while for only PET probe **4b** the SUV ratio was 3.02±0.327 (2.0 fold more than background). This result suggests that overall specific uptake by tumor compared with background about 5 fold more (2.0/0.4 = 5) at 24 h time point better than observed without blocking. At the end of 5 days pi, the NIRF imaging indicated very little change compared to that of 2 days pi, suggesting good retention of the probe in tumor with significant contrast between tumor and noncancerous tissues over time. It should be noted here that for NIRF imaging the concentration of probe 4a administered to mouse is significantly higher (10 nmol) than that of PET probe 4b (~0.065 nmol). These observations suggest that PET imaging has better sensitivity compared with fluorescence imaging and provides more accurate and quantitative analysis of tumor. On the other hand, NIRF imaging offers high throughput *in vivo* probe screening and therapy evaluation along with qualitative *ex vivo* tissue analysis at the microscopic level (Fig. 5) [38]. The development of a dual modality imaging probe is thus preferable for a comprehensive understanding of the disease state [12, 13].

Probe **4b** accumulated selectively in tumor with respect to post injection time and tumor weight, while it achieved steady state distribution quickly in organs such as heart, liver, lungs, and kidney (Fig. 4a and Fig. 4c). A very good correlation of tumor specific uptake of probe with respect to tumor size irrespective of the individual mouse was observed in this tumor model (Fig. 4c). Interestingly the dual-modality molecular imaging probe **4b** was observed to be present mainly in live tumor cells and not in necrotic and dead tumor cells (Fig. 5). This observation suggests that the probe **4b** can be used to detect live tumor cells and potentially offers a new tool for distinguishing live from dead cancer cells that could have significant utility in preclinical trials of drugs using animal models.

## CONCLUSION

The dual-modality molecular imaging probe PC-1001 described in the current study has demonstrated its applicability for tumor detection and quantitative image analysis in a mouse breast cancer model. The probe PC-1001 is accumulated specifically in cancerous tissue with good contrast to normal tissue. This probe could be useful in assisting the evaluation of anti-cancer therapies, anti-cancer drug discovery, and cancer-related biological studies. Further biological and toxicological evaluation of this imaging agent is ongoing, with the aim of advancing into pre-clinical studies.

## Supplementary Material

Refer to Web version on PubMed Central for supplementary material.

## Acknowledgments

This work was supported by Dr. Dongfeng Pan’s gift fund. We thank Dr. Weibin Shi for providing the light microscope. We thank Drs. Stuart Berr and Bijoy Kundu for assistance with PET imaging facilities and analysis.

## Abbreviations and Symbols

| | |
|---|---|
| **PET** | positron emission tomography |
| **SPECT** | single photon emission computed tomography |
| **US** | ultrasound |
| **NIRF** | near infrared fluorescence |
| **DOTA** | 1,4,7,10-tetraazacyclododecane-1,4,7,10-tetraacetic acid |
| **MTT** | 3-(4,5-dimethylthiazol-2-yl)-2,5-diphenyltetrazolium bromide |
| **HPLC** | high-performance liquid chromatography |
| **MALDI-TOF-MS** | matrix-assisted laser desorption/ionization time-of-flight mass spectroscopy |
| **NMR** | nuclear magnetic resonance |
| **FBS** | fetal bovine serum |
| **HSA** | human serum albumin |
| **KH** | Krebs-Henseleit buffer |
| **PBS** | phosphate buffered saline |
| **iv** | intravenous injection |
| **ip** | intraperitoneal injection |

| | |
|---|---|
| **OATP** | organic anion transport peptide |
| **BSP** | bromosulfophthalein |
| **MHI-148** | (2-[2-[2-chloro-3-[2-[1,3-dihydro-3,3-dimethyl-1-(5-carboxypentyl)-2H-indol-2-ylidene]-ethylidene]-1-cyclohexen-1-yl]-ethenyl]-3,3-dimethyl-1-(5-carboxypentyl)- 3H-indolium bromide) |
| $E_x$ | excitation wavelength |
| $E_m$ | emission wavelength |
| **log *P*** | partition coefficient |
| **ROI** | region of interest |
| **SUV** | standard uptake value |
| **RBC** | red blood cell |
| **H&E** | hemotoxylin and eosin |
| **V** | viable tumor region |
| **N** | necrotic tumor region |
| **pi** | post injection |

## REFRENCES


1. van der Meel R, Gallagher WM, Oliveira S, O'Connor AE, Schiffelers RM, Byrne AT. Recent advances in molecular imaging biomarkers in cancer: application of bench to bedside technologies. Drug Discov Today. 2010; 15:102–14. doi:10.1016/j.drudis.2009.12.003. [PubMed: 20035896]
2. Kaur S, Venktaraman G, Jain M, Senapati S, Garg PK, Batra SK. Recent trends in antibody-based oncologic imaging. Cancer Lett. 2012; 315:97–111. doi:10.1016/j.canlet.2011.10.017. [PubMed: 22104729]
3. Leonard F. Imaging and cancer: A review. Mol Onco. 2008; 2:115–52. doi:10.1016/j.molonc.2008.04.001.
4. Etzioni R, Urban N, Ramsey S, McIntosh M, Schwartz S, Reid B, et al. The case for early detection. Nature Reviews Cancer. 2003; 3:243–52. doi:Doi 10.1038/Nrc1041.
5. Glunde K, Pathak AP, Bhujwalla ZM. Molecular–functional imaging of cancer: to image and imagine. Trends Mol Med. 2007; 13:287–97. doi:10.1016/j.molmed.2007.05.002. [PubMed: 17544849]
6. Blasberg RG. Imaging Update: New Windows, New Views. Clin Cancer Res. 2007; 13:3444–8. doi:10.1158/1078-0432.ccr-07-0936. [PubMed: 17575206]
7. Ozkan E, Soydal C, Araz M, Kir KM, Ibis E. The role of 18F-FDG PET/CT in detecting colorectal cancer recurrence in patients with elevated CEA levels. Nucl Med Commun. 2012; 33:395–402. 10.1097/MNM.0b013e32834f7dbe. [PubMed: 22367859]
8. Phelps ME. Positron emission tomography provides molecular imaging of biological processes. Proc Nat Acad Sci. 2000; 97:9226–33. doi:10.1073/pnas.97.16.9226. [PubMed: 10922074]
9. Xiao L, Zhang Y, Liu ZQ, Yang M, Pu L, Pan DF. Synthesis of the Cyanine 7 labeled neutrophil-specific agents for noninvasive near infrared fluorescence imaging. Bioorg Med Chem Lett. 2010; 20:3515–7. doi:DOI 10.1016/j.bmcl.2010.04.136. [PubMed: 20488705]
10. Chen X, Conti PS, Moats RA. In vivo Near-Infrared Fluorescence Imaging of Integrin αvβ3 in Brain Tumor Xenografts. Cancer Res. 2004; 64:8009–14. doi:10.1158/0008-5472.can-04-1956. [PubMed: 15520209]
11. Luo S, Zhang E, Su Y, Cheng T, Shi C. A review of NIR dyes in cancer targeting and imaging. Biomaterials. 2011; 32:7127–38. doi:10.1016/j.biomaterials.2011.06.024. [PubMed: 21724249]

12. Wang W, Ke S, Kwon S, Yallampalli S, Cameron AG, Adams KE, et al. A New Optical and Nuclear Dual-Labeled Imaging Agent Targeting Interleukin 11 Receptor Alpha-Chain. Bioconjugate Chem. 2007; 18:397–402. doi:10.1021/bc0602679.
13. Cai W, Chen K, Li ZB, Gambhir SS, Chen X. Dual-Function Probe for PET and Near-Infrared Fluorescence Imaging of Tumor Vasculature. J Nucl Med. 2007; 48:1862–70. doi:10.2967/jnumed.107.043216. [PubMed: 17942800]
14. Chen K, Li Z-B, Wang H, Cai W, Chen X. Dual-modality optical and positron emission tomography imaging of vascular endothelial growth factor receptor on tumor vasculature using quantum dots. Eur J Nucl Med Mol Imaging. 2008; 35:2235–44. doi:10.1007/s00259-008-0860-8. [PubMed: 18566815]
15. Olson ES, Jiang T, Aguilera TA, Nguyen QT, Ellies LG, Scadeng M, et al. Activatable cell penetrating peptides linked to nanoparticles as dual probes for in vivo fluorescence and MR imaging of proteases. Proc Natl Acad Sci. 2010; 107:4311–6. doi:10.1073/pnas.0910283107. [PubMed: 20160077]
16. Weissleder R. Molecular Imaging in Cancer. Science. 2006; 312:1168–71. doi:10.1126/science.1125949. [PubMed: 16728630]
17. Yang X, Shi C, Tong R, Qian W, Zhau HE, Wang R, et al. Near IR Heptamethine Cyanine Dye-Mediated Cancer Imaging. Clin Cancer Res. 2010; 16:2833–44. doi:10.1158/1078-0432.ccr-10-0059. [PubMed: 20410058]
18. Yue W, Wang J-P, Hamilton CJ, Demers LM, Santen RJ. In Situ Aromatization Enhances Breast Tumor Estradiol Levels and Cellular Proliferation. Cancer Res. 1998; 58:927–32. [PubMed: 9500452]
19. Cui Y, Konig J, Leier I, Buchholz U, Keppler D. Hepatic Uptake of Bilirubin and Its Conjugates by the Human Organic Anion Transporter SLC21A6. J Biol Chem. 2001; 276:9626–30. doi:10.1074/jbc.M004968200. [PubMed: 11134001]
20. Yamaguchi H, Okada M, Akitaya S, Ohara H, Mikkaichi T, Ishikawa H, et al. Transport of fluorescent chenodeoxycholic acid via the human organic anion transporters OATP1B1 and OATP1B3. J Lipid Res. 2006; 47:1196–202. doi:10.1194/jlr.M500532-JLR200. [PubMed: 16534140]
21. Yue W, Zhou D, Chen S, Brodie A. A New Nude Mouse Model for Postmenopausal Breast Cancer Using MCF-7 Cells Transfected with the Human Aromatase Gene. Cancer Res. 1994; 54:5092–5. [PubMed: 7923123]
22. Henary M, Pannu V, Owens EA, Aneja R. Near infrared active heptacyanine dyes with unique cancer-imaging and cytotoxic properties. Bioorg Med Chem Lett. 2012; 22:1242–6. doi:10.1016/j.bmcl.2011.11.070. [PubMed: 22177785]
23. Chen X, Peng X, Cui A, Wang B, Wang L, Zhang R. Photostabilities of novel heptamethine 3H-indolenine cyanine dyes with different N-substituents. J Photochem Photobiol A-Chem. 2006; 181:79–85. doi:10.1016/j.jphotochem.2005.11.004.
24. Blagosklonny MV, Pressler H, Sissung TM, Venzon D, Price DK, Figg WD. Expression of OATP Family Members in Hormone-Related Cancers: Potential Markers of Progression. PLoS ONE. 2011; 6:e20372. doi:10.1371/journal.pone.0020372. [PubMed: 21625523]
25. Wlcek. Expression of Organic Anion Transporter Polypeptides (OATPs) in Human Breast Carcinoma. Sci Pharm. 2009; 77:196. doi:10.3797/scipharm.oephg.21.SL-29.
26. Briasoulis E, Valentinos K, Loakim, Martin S, Andreas T, Ioannis S, et al. Expression of organic anion-transporting polypeptides 1B3, 1B1, and 1A2 in human pancreatic cancer reveals a new class of potential therapeutic targets. OncoTargets Ther. 2011; 27 doi:10.2147/ott.s16706.
27. Locke LW, Chordia MD, Zhang Y, Kundu B, Kennedy D, Landseadel J, et al. A Novel Neutrophil-Specific PET Imaging Agent: cFLFLFK-PEG-(64)Cu. J Nucl Med. 2009; 50:790–7. doi:DOI 10.2967/jnumed.108.056127. [PubMed: 19372473]
28. Liu S. Radiolabeled Multimeric Cyclic RGD Peptides as Integrin αvβ3 Targeted Radiotracers for Tumor Imaging. Molecular Pharmacolgy. 2006; 3:472–87.
29. Vāvere ALLJ. Cu-ATSM: a radiopharmaceutical for the PET imaging of hypoxia. Dalton Transactions. 2007; 21:4893–902. [PubMed: 17992274]

30. Höglund JSA, Antoni G, Gustavsson SÅ, LÅngström B, Ringheim A, Sörensen J, Ben-Ami M, Ziv I. 18F-ML-10, a PET tracer for apoptosis: first human study. Journal of Nuclear Medicine. 2011; 55:720–5. [PubMed: 21498526]

31. Kenny LM, Vigushin DM, Adil A-N, Safiye O, K. LS, Sami S, et al. Quantification of Cellular Proliferation in Tumor and Normal Tissues of Patients with Breast Cancer by [18F]Fluorothymidine-Positron Emission Tomography Imaging: Evaluation of Analytical Methods. Cancer Research. 2005; 65:10104–112. [PubMed: 16267037]

32. Fukuda H, Paredes S, Batlle AM. Tumor-localizing properties of porphyrins. In vitro studies using the porphyrin precursor, aminolevulinic acid, in free and liposome encapsulated forms. Drug Des Deliv. 1989; 5:133–9. [PubMed: 2577983]

33. Ben-Dror S, Bronshtein I, Wiehe A, Roder B, Senge MO, Ehrenberg B. On the correlation between hydrophobicity, liposome binding and cellular uptake of porphyrin sensitizers. Photochem Photobiol. 2006; 82:695–701. doi:2005-09-01-RA-669 [pii] 10.1562/2005-09-01-RA-669. [PubMed: 16435882]

34. Smith K, Malatesti N, Cauchon N, Hunting D, Lecomte R, van Lier JE, et al. Mono- and tri-cationic porphyrin-monoclonal antibody conjugates: photodynamic activity and mechanism of action. Immunology. 2011; 132:256–65. doi:10.1111/j.1365-2567.2010.03359.x. [PubMed: 21039468]

35. Donald PJ, Cardiff RD, He DE, Kendall K. Monoclonal antibody-porphyrin conjugate for head and neck cancer: the possible magic bullet. Otolaryngol Head Neck Surg. 1991; 105:781–7. [PubMed: 1787967]

36. Lucienne J-J. The targeted delivery of cancer drugs across the blood—brain barrier: chemical modifications of drugs or drug-nanoparticles? Drug Discov Today. 2008; 13:1099–106. doi: 10.1016/j.drudis.2008.09.005. [PubMed: 18848640]

37. Kratochwil NA, Huber W, Müller F, Kansy M, Gerber PR. Predicting plasma protein binding of drugs: a new approach. Biochem Pharmacol. 2002; 64:1355–74. doi:10.1016/s0006-2952(02)01074-2. [PubMed: 12392818]

38. Xiao L, Zhang Y, Berr SB, Chordia M, Pramoonjago P, Pu L, et al. A Novel Near-infrared Fluorescence Imaging Probe for in vivo Neutrophil Tracking. Mol Imaging. 2011; 11:1–11.

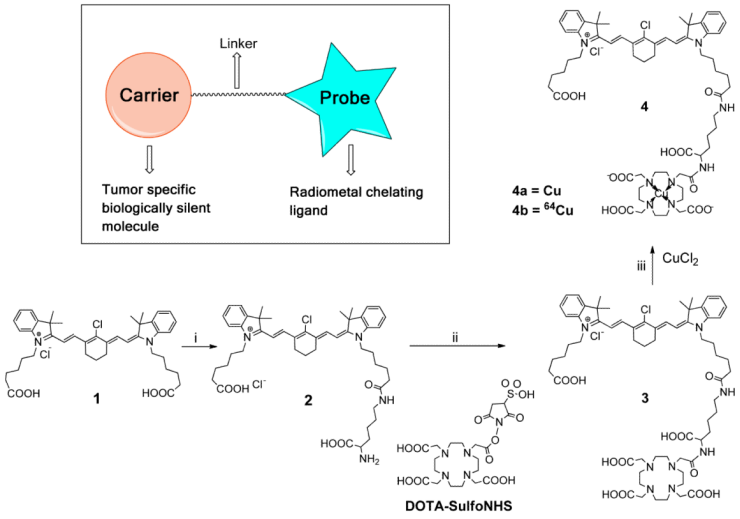


**Fig. 1.**

Design and synthesis of PC1001. Reagents and conditions: i, a. N-hydroxysuccinimide, DCC, $CH_2Cl_2$, rt,12 h; b. *t*Boc-lysine, 0.1 N sodium borate buffer, pH 8.5, 4° C, 12 h; c. pre-chilled 95% TFA, 4°C, 2 h. ii, DOTA-SulfoNHS (structure shown above), 0.1 N sodium borate buffer, pH 8.5, 12 h. iii, $CuCl_2$ or $^{64}CuCl_2$, DI $H_2O$, rt, 10 min.

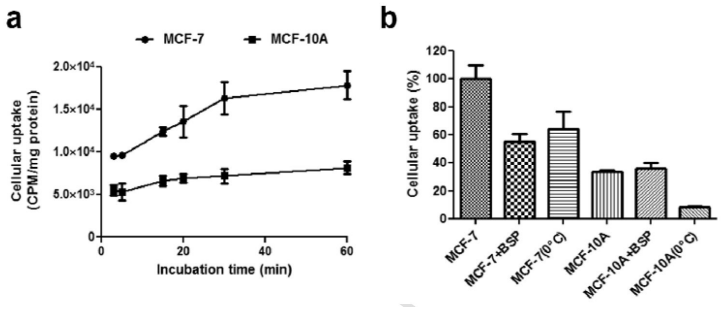


**Fig. 2.**

In vitro cellular uptake studies of **4b**. **a**) Time dependent cellular uptake in MCF-7B and MCF-10A cells. **b**) Mechanism-based cellular uptake in MCF-7B (shown as 7B) and MCF-10A (shown as 10A). BSP (OATP inhibitor) and 0°C were used to demonstrate the active transportation mechanism. Note: 37°C was used to incubate cells if not mentioned.

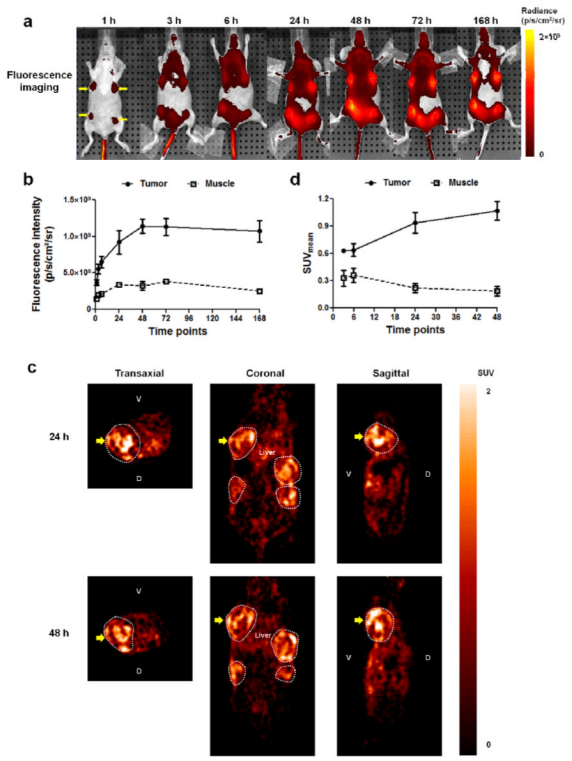


**Fig. 3.**

*In vivo* dual-modality fluorescence/PET imaging. **a**) Representative fluorescence imaging of mice at various time points (1, 3, 6, 24, 48, 72 and 168 h pi) post probe **4a** (10 nmol per 20 g mice) injection (iv). Four tumor sites are indicated with yellow arrows. **b**) Fluorescence intensities of tumor and muscle were plotted against post injection time (1 h up to 168 h pi) ($n$=4, $n_t$=16). **c**) Representative PET images of tumor-bearing mice ip administered with probe **4b**. Images are presented in three directions (transaxial, coronal and sagittal) at 24 and 48 h pi. Tumor regions are surrounded by white dotted circles. The tumor-of-interest in all images is indicated with bold yellow arrows. **d**) Mean SUV values of tumor and muscle at various time points (3, 6, 24 and 48 h pi).

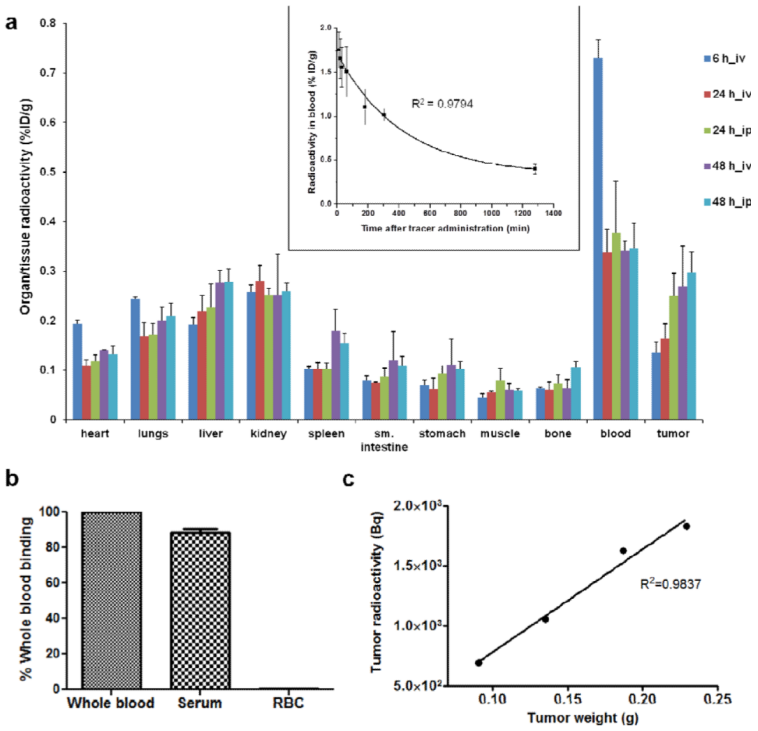


**Fig. 4.**

Pharmacokinetic/pharmacodynamic properties of PC1001 **4b**. **a**) Organ and tissue distribution of PC1001 at various time points (6, 24, and 48 h pi) and via different administration routes (ip vs. iv) ($n$=4 per group). Top inset, blood clearance profile of PC1001. Equation $y = y_0 + A_1 \times \exp[-(x-x_0)/t_1$ was used to fit the data points and the blood half-life was calculated to be 4.3±0.2 h ($n$=3) ($R^2$ = 0.9794 by Origin). **b**) Blood distribution of PC1001 at 6 h pi suggested that about 90% of probe was binding to serum instead of red blood cells (RBC) ($n$=3). **c**) Representative linear correlation ($R^2$=0.9837 by Origin) of PC1001 uptake by tumor radioactivity with tumor weight within a single mouse after 48 h.

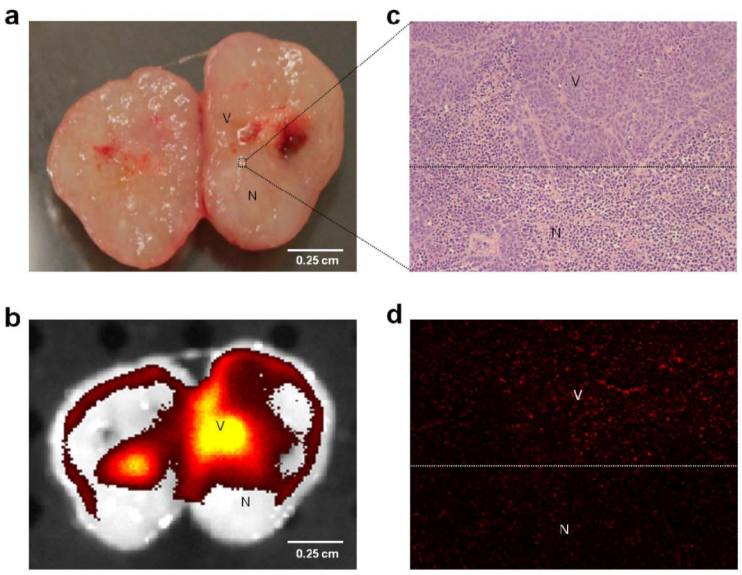


**Fig. 5.**

Probe distribution in tumor tissue at the microscopic level. **a**) Representative picture of freshly harvested tumor sectioned in half. Pink area could be observed as viable region (V) while necrotic (N) area was recognized as white or off-white color due to absence of blood supply. **b**) Fluorescence image (by IVIS spectrum) of the same tumor segment suggested that fluorescence signal (yellow) was mainly associated with viable regions. **c**) and **d**) demonstrated microscopic images of tumor area indicated by dotted line square (×100 fold magnification), which were also a zoomed-in version of panel **a** and **b**. While hemotoxylin/eosin staining (**c**) clearly exhibited the boarder of the viable and necrotic regions that were recognized by cell morphology, fluorescence microscopic image (**d**) revealed that the majority of fluorescence signal was associated with viable regions.